Digital rock physics benchmarks—Part I: Imaging and segmentation

Heiko Andrä [a,1], Nicolas Combaret [b,1], Jack Dvorkin [c,1], Erik Glatt [a,1], Junehee Han [d,1], Matthias Kabel [a,1], Youngseuk Keehm [d,1], Fabian Krzikalla [c,*,1], Minhui Lee [d,1], Claudio Madonna [e,1], Mike Marsh [b,1], Tapan Mukerji [c,1], Erik H. Saenger [e,1], Ratnanabha Sain [f,1], Nishank Saxena [c,1], Sarah Ricker [a,1], Andreas Wiegmann [a,1], Xin Zhan [f,1]

[a] Fraunhofer ITWM, Germany
[b] VSG, USA
[c] Stanford University, USA
[d] Kongju University, South Korea
[e] ETH Zürich, Switzerland
[f] ExxonMobil, USA

ARTICLE INFO

ABSTRACT

The key paradigm of digital rock physics (DRP) "image and compute" implies imaging and digitizing the pore space and mineral matrix of natural rock and then numerically simulating various physical processes in this digital object to obtain such macroscopic rock properties as permeability, electrical conductivity, and elastic moduli. The steps of this process include image acquisition, image processing (noise reduction, smoothing, and segmentation); setting up the numerical experiment (object size and resolution as well as the boundary conditions); and numerically solving the field equations. Finally, we need to interpret the solution thus obtained in terms of the desired macroscopic properties. For each of these DRP steps, there is more than one method and implementation. Our goal is to explore and record the variability of the computed effective properties as a function of using different tools and workflows. Such benchmarking is the topic of the two present companion papers. Here, in the first part, we introduce four 3D microstructures, a segmented Fontainebleau sandstone sample (porosity 0.147), a gray-scale Berea sample; a gray-scale Grosmont carbonate sample; and a numerically constructed pack of solid spheres (porosity 0.343). Segmentation of the gray-scale images by three independent teams reveals the uncertainty of this process: the segmented porosity range is between 0.184 and 0.209 for Berea and between 0.195 and 0.271 for the carbonate. The implications of the uncertainty associated with image segmentation are explored in a second paper.

1. Introduction

The fundamental aim of rock physics is to discover, understand and model relations between remotely-sensed geophysical observables and in-situ rock properties. Conventional rock-physics models are based on either empirical relations from laboratory measurements or theoretical models based on idealized microstructures and calibrated with available measurements. These models have given important insights to understanding cross-property relations. However, these models are almost always over-simplified, with regard to the geometry they represent and, at times, with the physical interactions within the geometry. Moreover, different rock property models represent or characterize rock microstructure differently, thereby lacking commonality and making cross-property analyses difficult.

Using high resolution representations of the complex pore geometry, digital rock physics has rapidly emerged as a potential source of valuable rock property relations (e.g., elastic, transport, and electrical properties) and fundamental understanding of pore-scale processes governing these properties. Its main principle is "image-and-compute" aimed at imaging 3D geometry of the mineral phase and the pore-space of a rock and then computationally simulating physical processes in this digital object: fluid flow to quantify permeability, electrical current flow to quantify resistivity, and elastic deformation to quantify elastic moduli and the elastic-wave velocity. With the advent of robust fine-resolution 3D imaging capability and software and hardware availability, digital rock physics is set to be a game-changer.

A modern method to acquire images of pore geometries is the micro-scale x-ray computed tomography (μxCT). The method enables the measurement of the local x-ray absorption within a

* Correspondence to: Department of Geophysics, Stanford University, Stanford CA 94305-2215, USA. Tel.: +1 650 723 0773; fax: +1 650 723 1188.
E-mail address: krz@stanford.edu (F. Krzikalla).
[1] Authors in alphabetical order.

small, cylindrical rock sample, with a typical diameter of a few millimeters or less. Three-dimensional images are reconstructed from a large number radiographs, i.e. projections of the imaged object, obtained at different projection angles. The result of the reconstruction is a grayscale image, where the brightness is proportional to the CT-number of the material within the object (Mees et al., 2003). A source of x-rays is available at synchrotron research facilities. Commercial μxCT scanners use x-ray tubes as a light source.

A cornerstone of the digital rock physics workflow is the segmentation of the scanned 3-D rock object. Segmentation refers to the identification and labeling of pore and mineral phases within the image. Due to the size of the 3-D data sets, manual segmentation is usually not feasible and image processing algorithms are required to automatically perform this task. Common image processing tools for 3-D segmentation are spatial filtering, noise and artifact removal, thresholding, morphological operations and cluster analysis. The segmentation of a grayscale image is not unique and segmentation algorithms therefore require manual interaction and quality control. For a review of image segmentation methods applied to porous media, we refer to Sezgin and Sankur (2004) or Iassonov et al. (2009).

An alternative way of obtaining three-dimensional images of rock microstructures is based on stochastic methods and is sometimes referred to as 2D-to-3D reconstruction (e.g. Liang et al., 2000; Keehm et al., 2003). The idea of this method is to estimate statistical properties of a rock sample from a two-dimensional image, such as obtained from scanning electron microscopy. The advantage of this approach is the possibility to generate a large number of digital samples with similar microstructural properties. The images thus produced, however, do not capture the complexity of natural rock samples, which limits their range of applications. In an attempt to generate pore geometries that more closely represent the fabrics of sedimentary rocks, so-called process-based methods have been developed. Those methods simulate or mimic the physical and geological processes that are acting during the rock genesis (Øren and Bakke, 2002).

As digital rock physics becomes more adopted in the geosciences and engineering, there is a critical need to establish benchmark datasets that researchers can use for testing and validating property-estimation algorithms and codes. In this paper, we describe four benchmark digital datasets: a Fontainebleau sandstone image, a Berea sandstone image, a Grosmont carbonate image, and a pack of spherical beads. The first three datasets consist of high resolution CT-scans, examples of segmentation and thresholding of the intensity data. The fourth dataset, the bead pack, was prepared by discretizing a random close pack on a regular 3D lattice. The initial random close pack was constructed using a granular dynamics simulation. We believe these datasets provide important benchmark model geometries for the digital rock physics community.

2. Imaging of benchmark datasets

2.1. Fontainebleau sandstone

The Fontainebleau sandstone dataset was acquired using the synchrotron source at Brookhaven National Laboratory by Exxon-Mobil and has been used in pioneering digital rock studies (e.g. Olson and Rothman, 1997; Lindquist et al., 2000). Fontainebleau sandstone consists mainly of monodisperse quartz sand grains. We provide the image segmented binary data (288 × 288 × 300) with grain and pore voxels (Fig. 1), unlike our other benchmark datasets which are available as raw images. The laboratory measured porosity is 0.152, and permeability is around 1100 mD (Keehm,
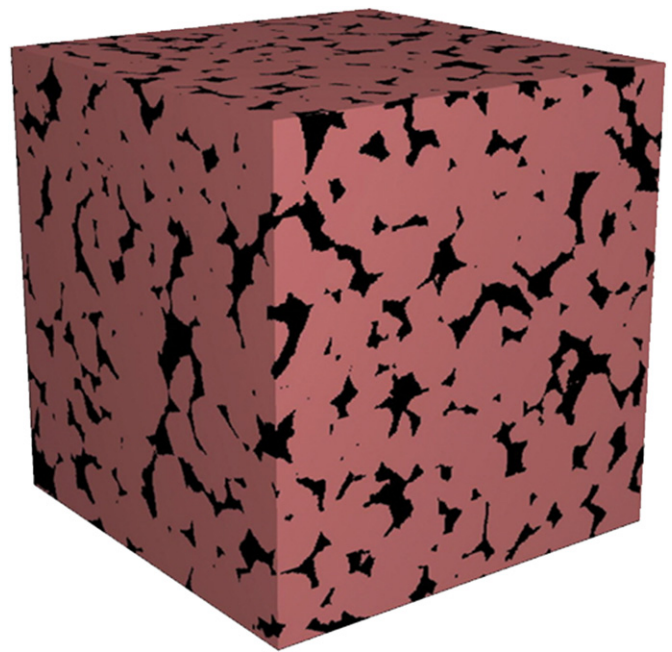

Fig. 1. The Fontainebleau sandstone dataset with a binary segmentation. The total size of the dataset is 288 × 288 × 300 and a voxel edge length is 7.5 μm.
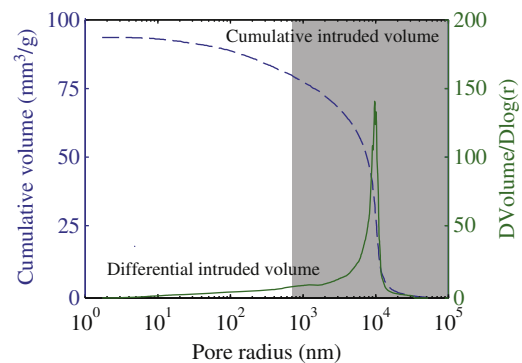

Fig. 2. Pore size distribution of the used Berea sandstone determined by mercury intrusion (after Madonna et al., 2012). The region marked with the grey shading can be resolved with the applied synchrotron-based X-ray tomographic microscopy.

2003). The P-wave velocity of a sample with the similar porosity under 1 MPa effective pressure is 4750 m/s (Han, 1986) and the formation factor is 32 (Fredrich et al., 1993).

2.2. Berea sandstone

For the imaging of Berea sandstone, we use a sample from the Berea SandstoneTM Petroleum Cores (Ohio, USA). To determine porosity, we performed helium and mercury porosimetry using a Helium Pycnometer 1330 (Micromeritics Instrument Corp., Belgium) and a Pascal 140+440 Mercury Porosimeter (Thermo Electron Corporation, Germany), respectively. Mercury porosimetry measurements were performed as described by Giesche (2006). The result is shown in Fig. 2 and the connected porosity is around 0.20. Permeability as provided by the company Berea SandstoneTM Petroleum Cores (Ohio, USA) is between 200 and 500 mD. We confirmed the mineral composition with petrographic microscopy and electron microprobe (Fig. 3). The results of a mineral texture analysis (Madonna et al., 2012) show that the solid matrix material of the Berea sandstone sample can be treated as an isotropic elastic solid, as the calculated velocity

anisotropy is less than 1%. Madonna et al. (2012) measured the ultrasonic P-wave velocities. They reported measured velocities over a range of confining pressure from 5 to 230 MPa using the pulse transmission technique (Birch, 1960; Christensen, 1965) at 3 MHz. The P-wave velocity varies from 2300 m/s at 5 MPa to 4000 m/s at 230 MPa.

We acquired the Berea sandstone dataset at the TOMCAT (Tomographic microscopy and coherent radiology experiments; Stampanoni et al., 2006) beamline at the Swiss Light Source (Paul Scherrer Institute, Villigen, Switzerland). The beam energy was optimized for best contrast. Transmitted X-rays were converted into visible light by a 20 μm Ce-doped LAG scintillator screen (Crytur, Czech Republic). Projections were magnified by microscope optics and digitized by a high-resolution CCD camera (PCO.2000). The beam energy was set at 26 keV and the exposure time was 500 ms with a magnification of $10\times$. The resulting image cube consists of $1024 \times 1024 \times 1024$ elements with a voxel edge length of 0.74 μm.
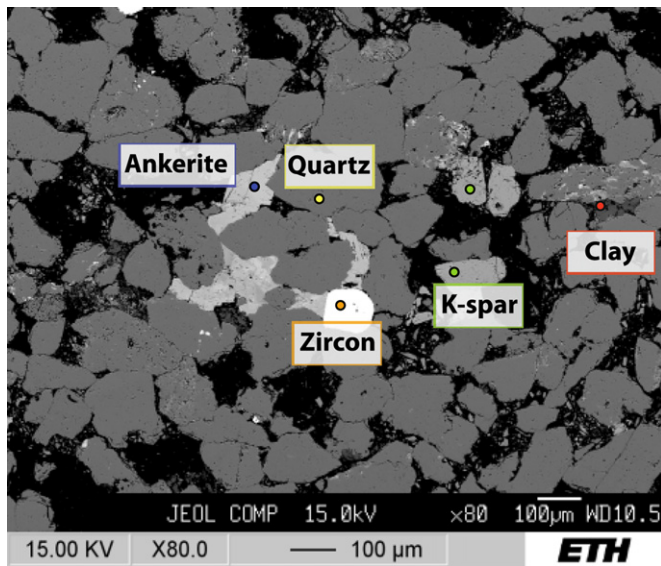

Fig. 3. Scanning Electron Microscopy (SEM) image of a Berea sandstone sample (after Madonna et al., 2012).

We reconstructed the tomographic volume using a highly optimized algorithm based on Fourier methods (Marone et al., 2009). The digital sample was produced from a cylindrical cores with a diameter of 2 mm, that was a fragment of a larger block (Ketcham and Carlson, 2001).

2.3. Carbonate

We obtained the carbonate sample from the Grosmont formation, Alberta, Canada. The area is known for bitumen reservoirs with tar sands and bitumen carbonates. The Grosmont formation was deposited during upper Devonian and can be divided into four members, LG, UG-1, UG-2, and UG-3 from the bottom. Two upper members (UG-2 and UG-3) were mostly composed of dolomite and karst breccia by diagenesis and karstification during late Devonian and late Jurassic (Buschkuehle et al., 2007). The sample comes from the UG-2 member. The lab-measured porosity is 0.21 porosity units, and permeability ranges from 150 mD to 470 mD. The P-wave velocity is obtained from well-log data and ranges from 2850 to 3850 m/s. We do not have a measurement of the electrical formation factor. The interval from which the sample comes is highly heterogeneous and we expect the properties to significantly vary from location to location.

We acquired the carbonate dataset at the high-resolution X-ray computed tomography facility at the University of Texas at Austin with an Xradia MicroXCT-400 machine. The facility used $4\times$ objective lenses, a 70 kV energy x-ray beam, and a 25 mm detector. The dataset was reconstructed with a beam hardening parameter of 0.4. The resulting image volume consists of $2048 \times 2048 \times 1932$ with a voxel edge length of 2.02 μm. Fig. 4 shows a 2D slice of the tomographic image alongside a blue-epoxy impregnated thin-section from the same sample. We cropped the original volume and created a $1024 \times 1024 \times 1024$ cube for further segmentation and property simulations.

2.4. Sphere pack

Packs of spherical grains are classical models of porous media and can serve as reasonable proxies for sedimentary granular geomaterials. In contrast to the sandstone (Fontainebleau and Berea) and carbonate images used in this study, we computationally
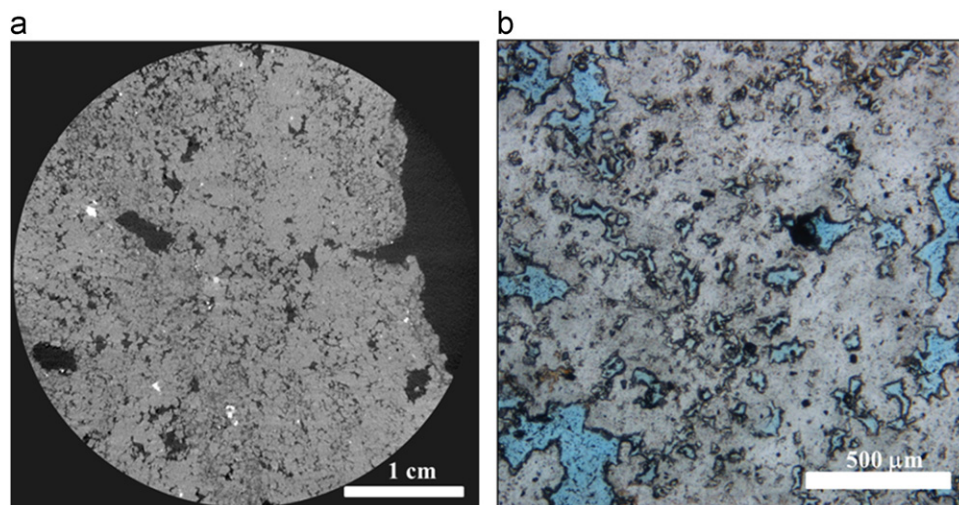

Fig. 4. (a) A 2D cross-sectional view of carbonate tomographic image with 2.02 μm voxel spacing and (b) a thin section image with blue-epoxy impregnation of the same carbonate sample.
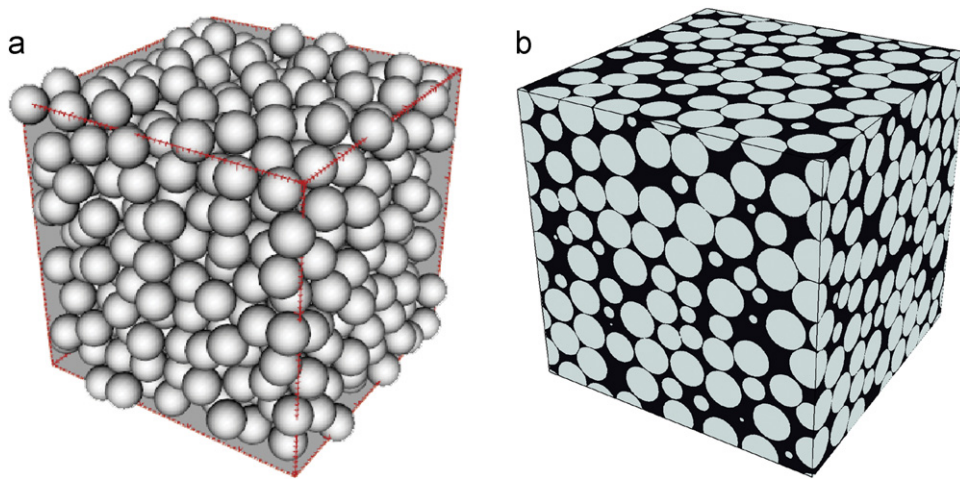
Fig. 5. Discrete (a) and discretized (b) images of the sphere pack geometry. The voxel size is 7 μm, the sphere diameter is 700 μm and the total image size of the binarized model is 788 × 791 × 793 voxels.

construct a random sphere pack using granular dynamics discrete element simulation.

The generation of the bead pack follows Sain (2010) and consists of the following steps: A square box is populated randomly with 621 non-overlapping equally-sized spheres with a diameter of 350 μm. Gradually reducing the box size leads to a rearrangement of the spheres, at the end of which the sphere ensemble forms a jammed pack. Subsequently, a global strain is applied to the ensemble, and spheres interact with the neighboring spheres through Hertz–Mindlin contact forces (Hertz, 1881; Mindlin and Deresiewicz, 1953; Johnson, 1987). This process allows for sliding and rotational sphere rearrangement and is continued until an average isotropic stress of 10 MPa is reached. At this reference state, the grains are at force equilibrium with neighboring grains. Further, the average coordination number (i.e., the average number contacts per grain) is 6.225 and porosity is 0.343. We use periodic boundary conditions throughout the simulation process. A further infinitesimal strain is applied to estimate a bulk modulus of 1.15 GPa and a shear modulus of 1.25 GPa. We will later refer to those values as reference elastic moduli.

We discretized the sphere pack on a uniform Cartesian grid. For this purpose, every voxel is identified as solid if the voxel center is less than one grain radius away from the nearest sphere center. All other voxels are identified as pore space. We neglect all deformations of the spheres due to elastic interactions between neighboring spheres, after confirming that incorporating the contact deformation (Horn et al., 1987) affects an insignificant number of voxels. The sphere pack was sampled using a voxel length of 7 μm, corresponding to 100 voxels per grain diameter and resulting in a total image volume of 788 × 791 × 793 voxels. Visualizations of the pack are shown in Fig. 5.

3. Image processing and segmentation

The second step in the digital rock physics workflow is the segmentation of the raw images. The purpose of this step is to remove artifacts of imaging, such as concentric shadows in the CT image and to delineate pores and minerals. Simple brightness thresholding is often not adequate for this purpose and, in this case, advanced image processing, such as noise reduction, artifact removal and multiband thresholding need to be utilized (Iassonov et al., 2009). This step is key to the success of estimating physical properties, which is the third step in the workflow. Improper segmentation

results in misidentification of pore-space (the pathways for fluid flow) and mineral-space (the stress bearing framework).

In the following sub-sections, we describe segmentation processes as performed by three research groups: VSG, Stanford University and Kongju University. We will subsequently refer to the VSG segmentation as the reference segmentation. All segmentations are based on the CT scan images of Berea sandstone and carbonate, shown in Fig. 6 with the grayscale histograms given in Fig. 7.

3.1. Reference segmentation (VSG)

The Berea sandstone sample suffered from reconstruction artifacts, some of which likely arose as part of the local tomography method used. The four most prominent artifacts were noise, streaks, brightness non-uniformity, and phase-contrast fringes at the grain edges. The noise was mitigated by using the non-local means image smoothing filter (Buades et al., 2005). There were significant streak artifacts that were seen only beyond the central z-axis cylinder. These streaks were excluded from analysis by applying a cylindrical mask which excluded all areas whose radius was greater than 512 pixels (378.88 μm).

Voxels closer to the center of the cylinder were systematically brighter than the distal voxels. To characterize the brightness inhomogeneity, a brightness profile was assembled and corrected. First, a few seed-voxels of pore-space were selected and then expanded with a region-growing tool; this produced a large sampling of pore-space voxels of varying brightness that extended throughout the reconstructed volume. Next, this selection was eroded by two pixels to exclude any phase-contrast darkened fringes near grain boundaries. Then a second-order polynomial was fit to the observed intensities; this polynomial defined the brightness profile. Image intensities were then scaled to normalize the brightness profile.

Interface areas are often difficult to label correctly by thresholding so a three-stage process was used to improve the labeling fidelity in boundary areas. In the first stage, the gradient magnitude of the image was computed and then thresholded to identify all boundaries (which appear very bright in the gradient magnitude image). These boundary voxels are marked to be excluded from consideration in the second stage. For the second stage, the dark pixels of the pore space were thresholded, and the bright pixels of mineral were thresholded. All pixels at or near the grain–pore interface were excluded from these selections in the second stage but are captured in the third stage by watershed expansion.
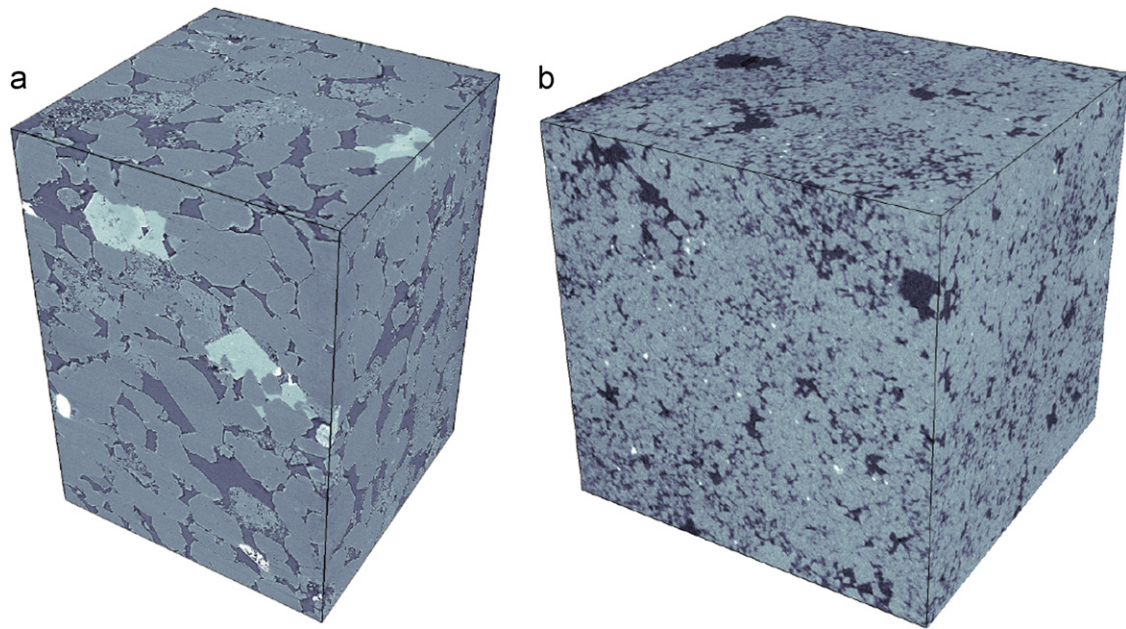
Fig. 6. CT scan volumes of (a) Berea sandstone, (b) carbonate sample. Both have the size of $724 \times 724 \times 1024$ and $1024 \times 1024 \times 1024$, respectively.
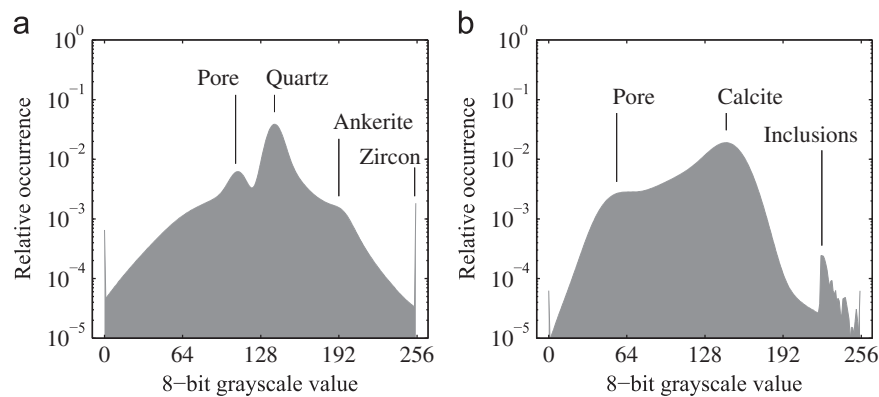

Fig. 7. Histograms of the grayscale values of Berea sandstone (a) and carbonate (b).

Each of these two selections from the second stage were then used as markers for a marker-based watershed algorithm (Beucher and Meyer, 1993), and the gradient magnitude image was used as the landscape input to the algorithm. The resulting watershed expansion completed the three-phase segmentation. This yielded a porosity of 0.184.

Like the sandstone sample, the carbonate sample exhibited brightness inhomogeneity and noise. The noise was smoothed by applying the same non-local means filter. The brightness inhomogeneity was addressed with the same solution of fitting and correcting the brightness profile, but two iterations of correction were applied instead of just one.

The sample exhibited porosities of varying scale including nano-scale pores which, due to convolution artifacts, were not as dark as larger pores. The segmentation approach was adjusted to correctly account for these voxels which were locally darker than the surrounding mineral, but not dark enough to be detected by simple thresholding.

The pore space was identified in two steps. In the first step, a global threshold was used to identify all globally dark areas, which included all large pores. To identify pores that were small, the black tophat transform of the image was computed, and its dark pixels were identified by interactive thresholding. The large

pores identified in the first step were merged with the small pores identified in the second step by applying a simple union of the two binary images. The resulting image was a map of all of the pore space; when inverted, the image produced the binary segmentation of all of the mineral space. This segmentation puts porosity at 0.247.

The results of the reference segmentation for the Berea sandstone and the vuggy carbonate sample are shown in Fig. 8. Both images depict subvolumes of $400 \times 400 \times 400$ voxels.

3.2. Stanford segmentation

We apply a three-step methodology to perform the image segmentation. First, the Berea sandstone and carbonate images are cropped laterally by 150 voxel layers to a cuboid of $724 \times 724 \times 1024$ voxels, in order to remove edge artifacts appearing in the image corners. Second, a threshold is chosen using Otsu's method (Otsu, 1979). We also perform manual thresholding to distinguish ankerite and zircon minerals from the quartz in the Berea image. The relative volume of these mineral inclusions is estimated at less than 2% of the mineral volume and is neglected in the further analysis. The segmented image contains small-scale features due to speckle noise. In a
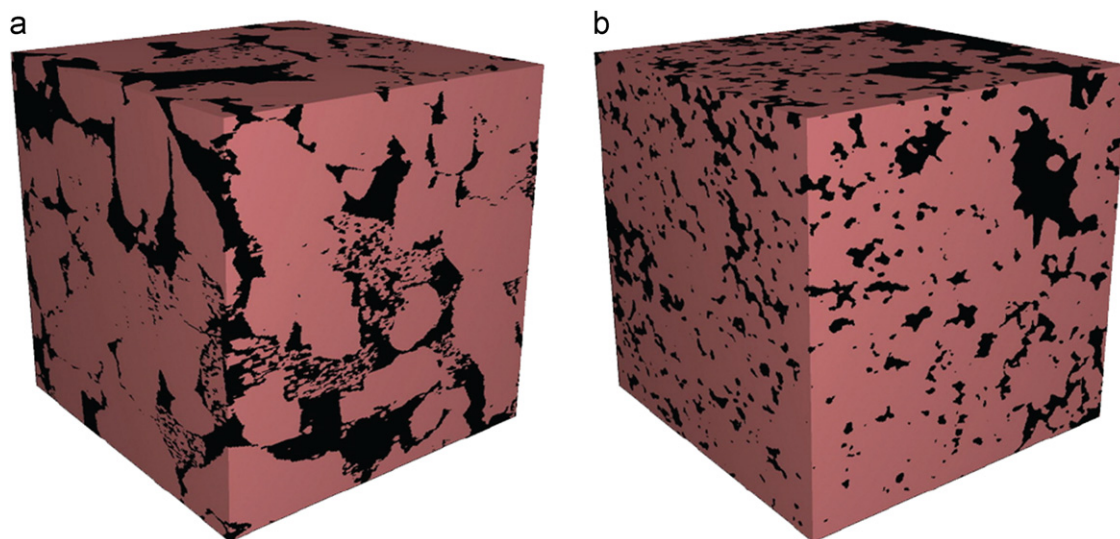
Fig. 8. Segmented sub-volumes of (a) Berea sandstone, (b) carbonate sample. Both have the size of 400 × 400 × 400. The length of Berea sub-volume is 2.96 mm and that of carbonate sub-volume is 8.08 mm.

third image segmentation step, those features are removed by relabeling all unconnected regions with a volume of less than 50 voxels using the color of the surrounding material. This segmentation results in porosities of 0.209 and 0.271 for the sandstone and the carbonate, respectively.

3.3. Kongju segmentation

For the segmentation of Berea and carbonate dataset, we apply a smoothing filter to reduce high-frequency noise from image reconstruction and single thresholding to distinguish minerals and pore space. We assume a mono-mineral composition, i.e. no classification of different minerals has been attempted. We do not perform any clustering analysis to find and remove isolated pore regions. After segmentation, porosities of Berea sandstone and carbonate sample are the same: 0.195 porosity units.

4. Discussion

The goal of segmentation is to identify all phases in an image correctly and distinctly. In most cases, the segmentation involves grayscale thresholding as a key step to distinguish between pore space and solid grains. The choice of segmentation algorithms, filtering parameters, and specifically the grayscale threshold, introduce an ambiguity to the process. Several methods exist that help choosing optimal thresholds (Sezgin and Sankur, 2004), but even if the image histograms reveal clearly distinct peaks in occurrence of one phase, as in the case of the Berea sandstone, the choice of the actual threshold value impacts significantly the resulting estimated sample porosity. Three different groups have performed segmentations and the porosity variation range is 0.209–0.184 (13% of the midrange porosity) in the case of the Berea and 0.271–0.195 (31% of the midrange porosity) in the case of the carbonate, see Table 1. The accuracy of the porosity prediction from digital images depends on the degree of available image resolution. Natural rock samples, in particular the carbonate sample shown in Fig. 6b, contain a significant amount of porosity at scales smaller than the size of the image voxels, which results in a blurring of the image and a smooth grayscale spectrum even if the sample mineralogy is simple.

Table 1
Porosities estimated using different segmentation procedures.

	Berea	Carbonate
KJ	0.195	0.195
SU	0.209	0.271
VSG	0.184	0.247
Midrange M	0.197	0.233
Range R	0.025	0.076
½R/M (%)	6.4	16.3

For the purpose of estimating effective properties, it is useful to characterize the pore geometry and to quantify the average size of the pores from the segmented images. Techniques that have been proposed for the analysis of porous media are medial axis (Goldak et al., 1991), pore connectivity (Lindquist and Venkatarangan, 1999), and the method of inscribed spheres (Silin and Patzek, 2006). Here, we restrict ourselves to computing the two-dimensional auto-correlation function for all horizontal slices of the Berea sandstone and the carbonate rock, which is a simple and robust way to characterize the predominant scales of random porous media. Correlation functions have also applications for the purpose of statistical 3-D reconstruction of porous media (e.g. Liang et al., 2000). Results of the correlation analysis are depicted in Fig. 9, alongside with the model functions that have been fitted to the average correlation function. We find that the auto-correlation of the Berea sandstone is reasonably well-described by an exponential function with a correlation length of 17 voxels. The autocorrelation function of the carbonate sample can be approximated using a superposition of two exponential correlation functions with correlation lengths of 5 and 70 voxels. In other words, the scale (in voxels) of large pores in the carbonate sample is about a factor of four larger than those of the Berea sandstone. At the same time, the carbonate image contains a significant amount of porosity with scales close to the limit of what can be resolved on the voxel grid. We note that all considered rock samples are inherently heterogeneous on the pore scale level and, therefore, petrophysical properties change from one digital image to another, even if they are extracted from the same core-sample.
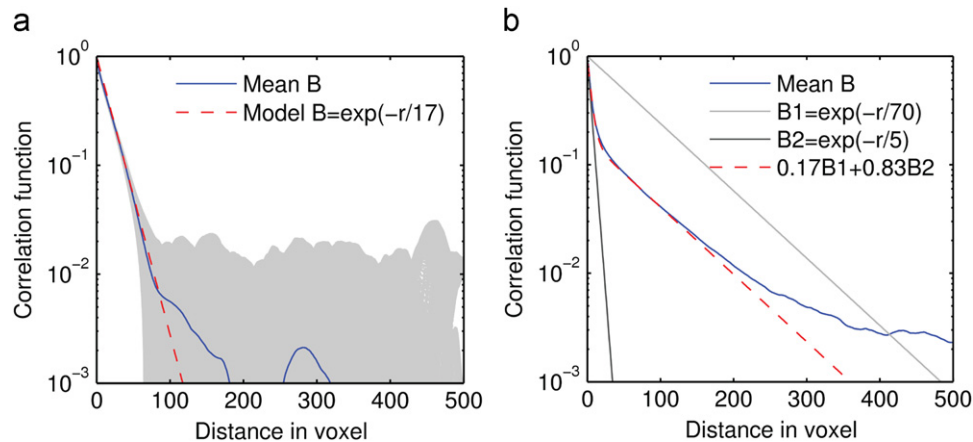
Fig. 9. Correlation length analysis for digital Berea sandstone sample (a), and a vuggy carbonate sample (b). The mean correlation function (blue solid line) is modeled using an exponential function for the sandstone, and a superposition of two exponential functions for the carbonate. (For interpretation of the references to color in this figure legend, the reader is referred to the web version of this article.)

5. Summary

We provide four digital images of porous rock microstructures as benchmark datasets for digital rock simulations. The imaged rock samples are Fontainebleau and Berea sandstone, a vuggy carbonate rock, and a computer-generated sphere pack.

For the Berea sandstone and for the carbonate sample, we provide different segmentations of the original grayscale image. Both images have a significant amount of sub-resolution porosity, and the porosity cannot be uniquely determined by the segmentation process. Three independent segmentations reveal variability in the porosity of segmented samples of 0.025 porosity units for Berea and 0.076 for the carbonate. The measured auto-correlation length of the Berea sandstone is 17 voxels, or 13 μm. The carbonate sample is characterized by two predominant length scales of 5 and 70 voxels, corresponding to 10 or 141 μm, respectively. For the Fontainebleau sandstone sample, we only provide the segmented image. The computer-generated sphere pack is digitized on a regular voxel grid with 100 voxels per sphere diameter.

The grayscale images of the Berea and carbonate samples, the coordinates of the spheres and reference segmentation of all four microstructure images are provided with the digital supplements of this paper for future benchmarking purposes. Part II of this work addresses the estimation of elastic, electrical and hydraulic properties derived from the rock microstructures presented here.

References

Beucher, S., Meyer, F., 1993. The morphological approach to segmentation: the watershed transformation. in: Dougherty, E.R. (Ed.), Mathematical Morphology in Image Processing, Marcel Dekker, NY, pp. 433–481.

Birch, F., 1960. The velocity of compressional waves in rocks to 10 kilobars. Part 1. Journal of Geophysical Research 65 (4), 1083–1102.

Buades, A., Coll, B., Morel, J.M., 2005. A non local algorithm for image denoising. In: Proceeding of the International Conference on Computer Vision and Pattern Recognition 2, pp. 60–65.

Buschkuehle, B.E., Hein, F.J., Grobe, M., 2007. An overview of the geology of the Upper Devonian Grosmont carbonate bitumen deposit, Northern Alberta, Canada. Natural Resources Research 16, 3–15.

Christensen, N.I., 1965. Compressional wave velocities in metamorphic rocks at pressures to 10 kilobars. Journal of Geophysical Research 70, 6147–6164.

Fredrich, J., Greaves, K., Martin, J., 1993. Pore geometry and transport properties of Fontainebleau sandstone. International Journal of Rock Mechanics and Mineral Sciences 30, 691–697.

Giesche, H., 2006. Mercury porosimetry: a general (practical) overview. Particle & Particle Systems Characterization 23 (1), 9–19.

Goldak, J.A., Yu, X., Knight, A., Dong, L., 1991. Constructing discrete medial axis of 3-D objects. International Journal of Computational Geometry & Applications 1 (3), 327–339.

Han, D., Nur, A., Morgan, D., 1986. Effect of porosity and clay content on wave velocity in sandstones. Geophysics 51, 2093–2107.

Hertz, H., 1881. Über den Kontakt elastischer Körper. Journal für die reine und angewandte Mathematik 92, 156–171. (in German).

Horn, R., Israelachvili, J., Pribac, F., 1987. Measurement of the deformation and adhesion of solids in contact. Journal of Colloid and Interface Science 115 (2), 480–492.

Iassonov, P., Gebrenegus, T., Tuller, M., 2009. Segmentation of X-ray computed tomography images of porous materials: a crucial step for characterization and quantitative analysis of pore structures. Water Resources Research 45, W09415.

Johnson, K., 1987. Contact Mechanics. Cambridge University Press 468 pp.

Keehm, Y., 2003. Computational Rock Physics: Transport Properties in Porous Media and Applications. Ph.D. Dissertation, Stanford University. 135 pp.

Keehm, Y., Mukerji, T., Nur, A., 2003. Permeability prediction from thin sections: 3D reconstruction and lattice-Boltzmann flow simulation. Geophysical Research Letters 31, L04606.

Ketcham, R.A., Carlson, W.D., 2001. Acquisition, optimization and interpretation of X-ray computed tomographic imagery: applications to the geosciences. Computer and Geosciences 27, 381–400.

Liang, Z., Ioannidis, M.A., Chatzis, I., 2000. Permeability and electrical conductivity of porousmedia from 3D stochastic replicas of the microstructure. Chemical Engineering Science 55 (22), 5247–5262.

Lindquist, W.B., Venkatarangan, A., 1999. Investigating 3D geometry of porous media images. Physics and Chemistry of the Earth 25 (7), 593–599.

Lindquist, W.B., Venkatarangan, A., Dunsmuir, J., Wong, T., 2000. Pore and throat size distributions measured from synchrotron X-ray tomographic images of Fontainebleau sandstones. Journal of Geophysical Research 105 (B9), 21509–21527.

Madonna, C., Almqvist, B.S.G., Saenger, E.H., 2012. Digital rock physics: numerical prediction of pressure-dependent ultrasonic velocities using micro-CT imaging. Geophysical Journal International 189 (3), 1475–1482. http://dx.doi.org/10.1111/j.1365-246X.2012.05437.x.

Marone, F., Hintermüller, C., McDonald, S., Abela, R., Mikuljan, G., Isenegger, A., Stampanoni, M., 2009. X-ray tomographic microscopy at TOMCAT. Journal of Physics: Conference Series 186, 012042 http://dx.doi.org/10.1088/1742-6596/186/1/012042.

Mees, F., Swennen, R., Van Geet, M., Jacobs, P., 2003. Applications of X-ray Computed Tomography in the Geosciences, 215. Geological Society, London, pp. 1–6 (Special Publications).

Mindlin, R., Deresiewicz, H., 1953. Elastic spheres in contact under varying oblique forces. Journal of Applied Mechanics 20 (3), 327–344.

Olson, J.F., Rothman, D.H., 1997. Two-fluid flow in sedimentary rock: simulation, transport and complexity. Journal of Fluid Mechanics 341, 343–370.

Øren, P.E., Bakke, S., 2002. Process based reconstruction of sandstones and prediction of transport properties. Transport in Porous Media 46, 311–343.

Otsu, N., 1979. A threshold selection method from gray level histograms. IEEE Transactions on Systems, Man and Cybernetics SMC-9, 62–66.

Sain, R., 2010. Numerical Simulation of Pore-Scale Heterogeneity and its Effects on Elastic, Electrical and Transport Properties. Ph.D. Dissertation, Stanford University, Stanford. 198 pp.

Sezgin, M., Sankur, B., 2004. Survey over image thresholding techniques and quantitative performance evaluation. Journal of Electronic Imaging 13 (1), 146–165.

Silin, D., Patzek, T., 2006. Pore space morphology analysis using maximal inscribed spheres. Physica A: Statistical Mechanics and its Applications 371 (2), 336–360.

Stampanoni, M., Groso, A., Isenegger, A., Mikuljan, G., Chen, Q., Bertrand, A., Henein, S., Betemps, R., Frommherz, U., Böhler, P., Meister, D., Lange, M., Abela, R., 2006. Trends in synchrotron-based tomographic imaging: the SLS experience. In: Proceedings of SPIE, The International Society for Optical Engineering, 6318, pp. M1–M14.